MEMS IMU/ODO-Aided GNSS Long Coherent Integration PLL for Urban Vehicle Precise Positioning

Tisheng Zhang, *Member, IEEE*, Huilin Shi, Liqiang Wang, *Graduate Student Member, IEEE*, Xin Feng, Yuepei Shi, and Xiaoji Niu, *Member, IEEE*

***Abstract*—Global navigation satellite system (GNSS) carrier phase measurement is highly vulnerable to signal attenuation, multipath, and blockage in urban environments, which significantly degrades the availability of precise GNSS positioning. Long coherent integration (LCI) serves as an effective approach to suppress thermal noise and mitigate multipath interferences within phase-locked loops (PLLs); however, its performance is constrained by the dynamic stress resulting from satellite–receiver motions. This study proposes a GNSS/inertial navigation system (INS)/odometer (ODO) deeply coupled (GIO-DC) system with LCI PLLs. An (ODO) distance increment measurement model is integrated with a MEMS IMU to estimate and compensate for the PLLs' dynamic stress with enhanced accuracy and reliability, thereby enabling extended coherent integration time. In addition, a four-quadrant phase discriminator is adopted to expand the PLL pull-in range and reduce the likelihood of cycle slips. Field tests on a wheeled vehicle in typical urban complex environments were conducted to evaluate the performance of the GIO-DC system from multiple perspectives. The results confirmed the superiority of the proposed approaches. A coherent integration time of 800 ms was achieved, realizing continuous carrier phase measurement and robust centimeter-level positioning. The proposed deeply integrated system, built on the low-cost MEMS IMU and ODO, delivers performance on par with that of a system based on a navigation-grade IMU.**

***Index Terms*—Carrier phase, deep integration, global navigation satellite system (GNSS)/inertial navigation system (INS)/odometer (ODO), long coherent integration (LCI), phase-locked loops (PLLs).**

Received 19 September 2025; revised 17 November 2025; accepted 26 November 2025. Date of publication 24 December 2025; date of current version 6 January 2026. This work was supported in part by the National Natural Science Foundation of China under Grant 42374034, in part by the Key Research and Development Program of Hubei Province under Grant 2024BAB024, in part by the Major JianDao (Sharp Sword) of Hubei Province under Grant 2023BAA02602, and in part by the High Quality Development Project of the Ministry of Industry and Information Technology (MIIT) under Grant 2024-182. The Associate Editor coordinating the review process was Dr. Alessio De Angelis. *(Corresponding authors: Xin Feng; Tisheng Zhang.)*

Tisheng Zhang, Huilin Shi, and Liqiang Wang are with the GNSS Research Center and the Electronic Information School, Wuhan University, Wuhan 430072, China (e-mail: zts@whu.edu.cn).

Xin Feng is with the GNSS Research Center, Wuhan University, Wuhan 430072, China, and also with the School of Electronic Science and Engineering, Chongqing University of Posts and Telecommunications, Chongqing 400065, China (e-mail: focusfeng@whu.edu.cn).

Yuepei Shi is with the School of Geodesy and Geomatics, Wuhan University, Wuhan 430072, China, and also with Hubei Luojia Laboratory, Wuhan 430079, China.

Xiaoji Niu is with the GNSS Research Center, Wuhan University, Wuhan 430072, China, and also with Hubei Luojia Laboratory, Wuhan 430079, China.

Digital Object Identifier 10.1109/TIM.2025.3648069

NOMENCLATURE

ESKF	Error-State Kalman Filter.
FLL	Frequency-locked loop.
GIO-DC	GNSS/INS/ODO deeply coupled.
IF	Intermediate frequency.
I/*Q*	In-phase and quadrature.
LCI	Long coherent integration.
NCO	Numerically controlled oscillator.
NHC	Nonholonomic constraint.
ODO	Odometer.
PLI	Phase lock indicator.
PLL	Phase-locked loop.
rms	Root mean square.
RTK	Real-time kinematic.
SNR	Signal-to-noise ratio.

I. INTRODUCTION

THE global navigation satellite system (GNSS) serves as a cornerstone for comprehensive positioning, navigation, and timing (PNT) systems by providing continuous, high-precision spatiotemporal reference information. It plays a critical role in various applications such as intelligent robots, traffic monitoring, and autonomous vehicles [1], [2]. High-precision GNSS positioning algorithms, including RTK, precise point positioning (PPP), and PPP-RTK, enable decimeter-level or even centimeter-level dynamic positioning accuracy through the use of carrier phase observations [3]. The availability of high-quality carrier phase observations relies heavily on the GNSS receiver's ability to maintain accurate and continuous signal tracking via its PLLs. However, GNSS signals are susceptible to attenuation, multipath, and blockage, making PLLs difficult to sustain stable signal tracking in challenging environments such as urban canyons or dense foliage canopies [4], [5]. These factors hinder the acquisition of precise carrier phase observations, thereby compromising the reliability and accuracy of positioning solutions. Therefore, overcoming these limitations is essential for precise GNSS positioning in dynamic and complex scenarios.

LCI in tracking loops can enhance the continuity and accuracy of carrier phase observations significantly. Compared to extending noncoherent integration time, extending the coherent integration time avoids the issue of squaring loss [6]. In complex environments, where signals are frequently attenuated, LCI fundamentally increases the signal energy and enhances

the SNR, thereby effectively improving the tracking sensitivity under degraded signal conditions [7], [8]. In addition, LCI enhances the resolution of multipath components with different frequencies, thereby aiding in the mitigation of multipath effects [9]. However, practical implementation of LCI is constrained by navigation bit sign transitions, oscillator instability, and satellite–receiver dynamics. The issue of navigation bit sign transitions can be addressed by employing unmodulated pilot signals, using external bit-aiding techniques, and utilizing bit estimation methods. As the coherent integration time increases, oscillator instability introduces phase errors that lead to signal energy loss, thereby degrading the performance of coherent integration. The impact of oscillator instability can be mitigated through difference-based [10] or estimation-based [7], [11] techniques. Moreover, LCI faces a tradeoff between dynamic stress and thermal noise. On the one hand, the user dynamics constitute one of the primary error sources that the tracking loop must handle. To support high-dynamic user motion, a wider loop bandwidth is required to enhance the loop's tolerance to frequency tracking errors induced by dynamic stress. On the other hand, longer coherent integration periods suppress thermal noise and enhance tracking precision [12]. However, longer coherent integration inherently requires a narrower tracking-loop bandwidth, increasing the impact of dynamic stress on the loop performance. As a result, the relative satellite–receiver dynamics become the primary factor that limits the extension of coherent integration time.

To address these challenges, deep integration of GNSS and the INS has emerged as an effective solution. GNSS provides precise long-term positioning but suffers from low update rates and vulnerability to environmental interference. Inertial measurement units (IMUs) offer high update rates, strong dynamic responsiveness, and good short-term accuracy, but their errors accumulate rapidly with time and eventually cause divergence. Their complementary characteristics enable mutual assistance [13], [14], and deep integration further enables the inertial system to aid GNSS at the signal level. By adopting GNSS/INS deep integration, the dynamic stress encountered in tracking loops can be compensated, allowing the loops to work under quasistatic conditions and enabling the realization of LCI [15], [16]. As mentioned above, if the oscillator instability is mitigated, the accuracy of dynamic stress estimation becomes the primary constraint on further extending the integration time, which is the core issue that this article aims to address.

Many studies have been conducted on LCI techniques for FLLs. Luo et al. [17], [18], [19] proposed a method based on the fractional Fourier transform (FRFT), projecting the signal into the FRFT domain to enable an ultra-LCI time without the need for external IMU assistance. This approach estimates the frequency rate variation caused by receiver dynamics purely through signal transformation. Ren and Petovello [20] utilized a maximum likelihood (ML) method to estimate navigation bits and implemented a GNSS/INS deeply integrated vector tracking structure, achieving a coherent integration period of up to 100 ms. Pany et al. [21] employed multisensor fusion to assist the tracking loop, enabling up to a 2 s of coherent integration time and successful tracking of signals as weak as 1.5 dB-Hz in dynamic environments. Cheng et al. [22] introduced a sensor-aided long integration (SALI) approach and allowed a coherent integration time of up to 1 s with sensor assistance, enabling the tracking of code phase and Doppler, along with effective multipath separation and mitigation. However, these studies primarily focus on improving the performance of pseudo-range and Doppler, without incorporating effective carrier phase aiding mechanisms.

A study [23] quantitatively assessed the effectiveness of inertial sensors of different grades in assisting PLLs. Compared to frequency and code tracking loops, PLLs are more sensitive to errors and more prone to loss of lock in challenging environments. As a result, PLLs impose stricter requirements on the accuracy of aiding information. Soloviev and Jeffrey Dickman [24] demonstrated the feasibility of long coherent carrier phase tracking in indoor weak-signal environments using consumer-grade IMUs. However, carrier phase observations were frequently interrupted, and high-precision positioning could not be achieved using these observations under dynamic conditions. Zhang et al. [25] used industrial-grade MEMS IMUs to assist loop tracking for LCI, showing that MEMS IMUs can alleviate the dynamic stress in tracking loops to some extent, realizing a 100 ms of coherent integration time, but the positioning errors were at the decimeter level. Dampf et al. [26] and Bochkati et al. [27] proposed synthetic aperture processing (SAP) schemes that utilize inertial sensors to measure and compensate for antenna motion. However, their approaches focused solely on bandwidth compression without extending the coherent integration time, and their experiments were conducted in open-sky environments without verifying the carrier tracking performance under signal-challenged conditions. Overall, research on LCI specifically for carrier phase tracking remains limited. Moreover, low-cost MEMS IMUs suffer from rapid error drift for their drawbacks concerning design principles and production processes [28], [29], making it difficult to maintain sufficient accuracy over extended coherent integration periods. The navigation-grade IMUs are capable of providing high-precision aiding information for their lower bias drift and superior noise characteristics. However, their use is often limited by cost constraints in practical applications.

As an inherent sensor on wheeled vehicles, the ODO provides distance increment information in the forward direction [30], effectively enhancing the dead reckoning performance of INS and suppressing error divergence. The integration of the MEMS IMU and ODO (INS/ODO) significantly enhances the accuracy of dynamic stress estimation, thereby enabling longer coherent integration time of PLLs. In terms of the ODO measurement model, the velocity measurement model [31], [32] represents the classical approach, whereas our previous study [33] introduced the distance increment measurement model. The study showed that the distance increment measurement model exhibits lower measurement error than the velocity measurement model. Moreover, in short-term GNSS outage tests, the forward positioning errors of the distance increment measurement model were statistically reduced by 67% compared to those of the velocity measurement model. Therefore, when applying INS/ODO to assist the PLLs for LCI, the distance increment measurement model is preferable.

Moreover, the signal will be sent to the phase discriminator to estimate the phase error after coherent integration. The discrimination result represents the time-averaged phase error

of the signal during the coherent integration period. The pull-in range of the traditional Costa two-quadrant phase discriminator is only $[-\pi/2, \pi/2]$ [34]. In complex environments, various interferences can induce phase errors exceeding $\pi/2$, causing the replica and received signals to shift from an unbiased estimate toward a π phase offset, or vice versa, ultimately resulting in half-cycle slips of the carrier phase. In more severe environments, such conditions may cause the tracking loop to lose lock entirely. Therefore, it is necessary to adopt a phase discriminator with a wider pull-in range to improve the loop's robustness.

Based on the rigid requirement of high-precision dynamic aiding information in PLL LCI, this article proposes a GIO-DC system. The system enhances the accuracy of aiding information by integrating a low-cost MEMS-IMU with a wheeled ODO distance increment measurement model. Additionally, a four-quadrant phase discriminator is used to extend the phase error detection range. This approach enables LCI tracking of the carrier phase in complex environments, providing continuous and stable carrier phase observations and positioning. This system can be applied to a variety of practical scenarios requiring continuous and reliable positioning, such as autonomous driving, precision agriculture, and intelligent urban navigation. These applications highlight the potential of the proposed method to enhance the robustness and accuracy of GNSS tracking in challenging environments.

The main contributions of this article are listed as follows.

1) A GIO-DC system with LCI PLLs is proposed, wherein a four-quadrant phase discriminator is employed to extend the pull-in range of the LCI PLLs, improving the stability of carrier phase tracking.
2) The integration information of a consumer-grade MEMS IMU and an ODO distance increment measurement model is employed to aid PLLs, enabling accurate estimation of dynamic stress and realizing PLLs' LCI. Meanwhile, the accuracy of the aiding information is quantitatively evaluated to verify its effectiveness in supporting LCI.
3) The impacts of phase discriminators, integration models, and coherent integration times on the LCI PLLs are thoroughly evaluated in dense foliage canopies scenarios. We can achieve an 800-ms coherent integration period and centimeter-level positioning accuracy with the aid of the proposed LCI PLLs, which are comparable to the results obtained utilizing navigation-grade inertial sensors.

II. Methodology

A. Overview of the GIO-DC System

Fig. 1 shows the architecture of the GIO-DC system. Each satellite's signal is processed in an independent tracking channel. The incoming IF signal is mixed and correlated with local replicas to produce 1-ms correlation outputs. For pilot channels, these results can be directly used for LCI, while nonpilot signals require bit wipe-off before coherent integration. The I/Q components of the LCI are fed into a phase discriminator that supports both two-quadrant and four-quadrant discrimination modes. In challenging environments, the four-quadrant phase discriminator is employed to improve tracking robustness. The estimated phase error is filtered and fed back to the NCO for continuous carrier phase replica adjustment.

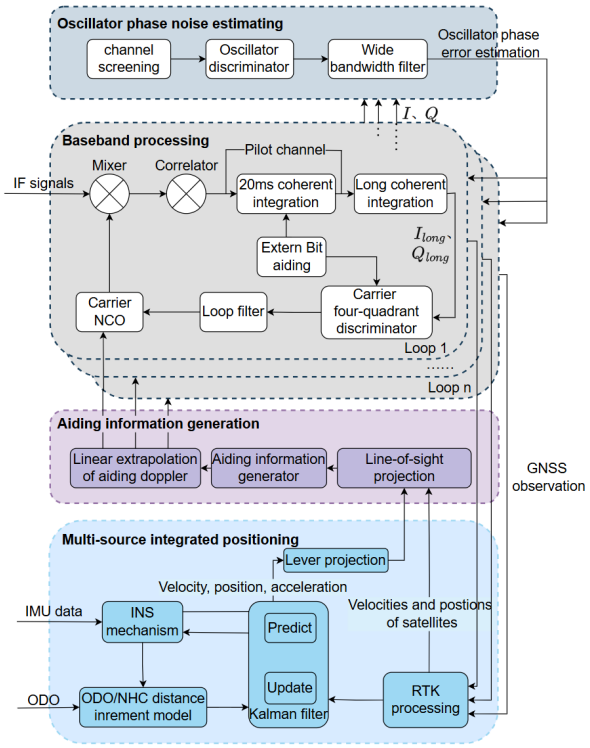

Fig. 1. Overview of the GIO-DC system.

Each tracking channel independently produces pseudo-range and carrier phase observations, which are jointly processed by an RTK module for precise positioning. Meanwhile, IMU and ODO measurements are processed separately: IMU data are utilized to propagate the system's navigation and error state estimates over time, while ODO readings and NHC are incorporated to formulate a distance increment measurement. These outputs, together with the RTK positioning results, are integrated with a Kalman filter. The Kalman filter ultimately outputs the vehicle's velocity, position, and acceleration, which are further projected to the antenna phase center via lever-arm compensation and then forwarded to the aiding information generation module.

We proposed the multichannel cooperative tracking loop to estimate the oscillator phase errors in our previous research [7], which is also employed in this system. The correlator values of different channels are utilized to estimate the clock phase errors jointly, which will be fed back into the channels' carrier phase NCO to mitigate the oscillator instability.

The relative motion between the receiver and satellites becomes the primary constraint as the coherent integration time increases. An aiding information generation module is designed to mitigate the loop dynamics. With the integrated GNSS/IMU/ODO navigation solution, the receiver's position, velocity, and acceleration can be accurately estimated, and the satellites' positions and velocities are computed through broadcast ephemeris during RTK processing. Based on both sets of dynamic information, the Doppler caused by the relative motion between the receiver and satellites can be

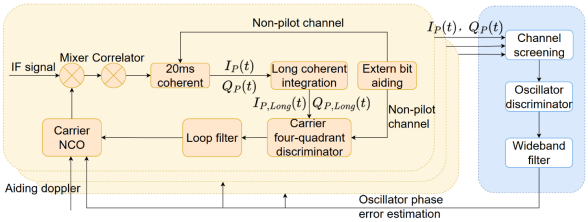

Fig. 2. Diagram of LCI carrier phase tracking.

estimated. To promptly compensate for the dynamic stress in the tracking loop, the aiding Doppler is linearly extrapolated and updated at a high rate, which will be injected into the loop NCO, effectively eliminating most of the dynamic stress. As a result, the tracking loop should only handle the residual dynamics, enabling further extension of coherent integration time.

To further demonstrate the practicality of the proposed architecture, we also evaluated its implementation complexity and real-time feasibility. Although the proposed system architecture contains multiple synchronized modules, its actual implementation is divided into two main subsystems: the GNSS baseband processing subsystem and the multisource fusion subsystem. The oscillator phase noise estimation module is embedded within the GNSS subsystem and has a negligible impact on overall throughput. The GNSS baseband processing has been widely validated to support real-time execution, while the fusion subsystem primarily involves linear computations with low computational overhead. Moreover, the aiding information is generated during time-synchronized data exchange, introducing negligible latency. Analysis indicates that all modules operate well within real-time constraints on typical vehicular processors, indicating that the proposed system is readily deployable in real-world high-throughput and large-scale urban navigation scenarios.

Sections II-B–II-D will provide a detailed description of the principles and implementation of each component in the proposed system architecture.

B. LCI Carrier Phase Tracking Design

As shown in Fig. 2, the LCI carrier phase tracking architecture is composed of the carrier phase tracking loop and the multichannel cooperative tracking loop. The former will process the input IF signal by a carrier mixer and a code correlator first, followed by a 20-ms short-term integration. The resulting in-phase $I_P(t)$ and quadrature $Q_P(t)$ signals are then forwarded to the LCI module and the multichannel cooperative tracking loop, respectively.

The multichannel cooperative tracking loop is designed to estimate the common oscillator phase error by jointly processing the correlator outputs from all channels. The loop chooses the suitable channels based on loop parameters such as the carrier-to-noise ratio and the satellite elevation, thereby ensuring that the channels employed for clock error estimation maintain low thermal noise levels. Since oscillator instability imposes identical effects on all channels, the oscillator discriminator derives an estimation of the clock-induced phase errors through averaging the measurements collected across all channels. The phase error output of each channel is derived from the product of the I/Q components, and the sum phase error output of all channels will be normalized by the signal amplitudes squared

$$\tilde{\theta}_e = \frac{\sum_{n=1}^{N} I^{(n)} Q^{(n)}}{\sum_{n=1}^{N} \left(I^{(n)}\right)^2} \tag{1}$$

where $\tilde{\theta}_e$ denotes the estimation of clock phase errors. $I^{(n)}$ and $Q^{(n)}$ are correlator values of different channels.

Compared to the local loops, the multichannel cooperative tracking loop employs a wideband filter to process the oscillator discriminator outputs, and the filtered results are fed into different local loops. This approach mitigates the influence of oscillator instability, leaving satellite–receiver dynamics and thermal noise as the dominant factors affecting LCI tracking performance.

For pilot channels, which are not modulated by navigation bits, the influence of bit sign transitions can be ignored. Therefore, the 1-ms correlation results can be directly accumulated to perform LCI. In contrast, for signals modulated by navigation bits, a bit wipe-off operation is applied to remove the modulated navigation data based on an external bit aiding source. The resulting bit-synchronized I/Q signals serve as the fundamental units for subsequent LCI. The I/Q outputs of the LCI module are then passed to a local phase discriminator for carrier phase error detection.

At this stage, the integrated in-phase signal $I_{P,\mathrm{Long}}(t)$ and quadrature signal $Q_{P,\mathrm{Long}}(t)$ can be expressed as

$$I_{P,\mathrm{Long}}(t) = A\cos(\omega_e t + \theta_e) \tag{2}$$

$$Q_{P,\mathrm{Long}}(t) = A\sin(\omega_e t + \theta_e) \tag{3}$$

where A represents the magnitude of the signal and ω_e and θ_e represent the carrier frequency offset and the initial phase difference between the input signal and the replica signal, respectively.

In tracking loops, the two-quadrant arc-tangent phase discriminator is one of the most commonly adopted techniques for phase error estimation due to its simplicity and effectiveness. The phase error output of the two-quadrant discriminator can be expressed as

$$\varphi_e(t) = \arctan\left(\frac{Q_{P,\mathrm{Long}}(t)}{I_{P,\mathrm{Long}}(t)}\right) \tag{4}$$

where $\varphi_e(t)$ denotes the phase error output of the discriminator, while $Q_{P,\mathrm{Long}}(t)$ and $I_{P,\mathrm{Long}}(t)$ represent I/Q components of the LCI signal, respectively.

When the actual phase errors lie within the range of $[-\pi/2, \pi/2]$, the output of the two-quadrant phase discriminator exhibits a linear relationship with the true phase error. Moreover, as shown in (2)–(4), the two-quadrant discriminator is inherently insensitive to the π carrier phase reversals caused by navigation bit sign transitions, making it well-suited for nonpilot signals without bit wipe-off. However, when the actual phase error exceeds $\pi/2$, the discriminator output becomes nonlinear and ambiguous. In such cases, the loop adjusts the replica carrier phase in the wrong direction, increasing the phase error and eventually leading to loss of lock [35].

The phase detection equation of the four-quadrant phase discriminator is given as

$$\varphi_e(t) = \arctan 2\left(Q_{P,\mathrm{Long}}(t), I_{P,\mathrm{Long}}(t)\right). \tag{5}$$

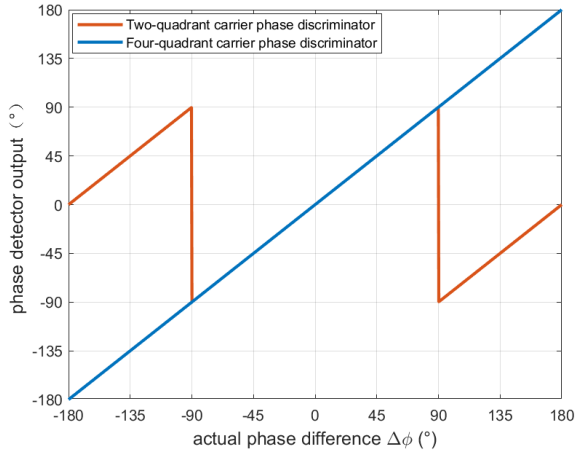

Fig. 3. Comparison of the two-quadrant and four-quadrant discriminators.

As shown in the above equation, the four-quadrant phase discriminator is sensitive to navigation bit sign transitions. When LCI is not employed, the external bit aiding source is employed to eliminate the influence of bit sign transitions before applying a four-quadrant phase discriminator. Compared to the two-quadrant method, the four-quadrant phase discriminator offers a doubled effective pull-in range. Fig. 3 illustrates a comparison of the phase detection characteristics of both methods, where the four-quadrant discriminator has a detection range of $[-\pi, \pi]$. In challenging environments, carrier phase errors often fall outside the linear pull-in range of the two-quadrant discriminator, but remain within $[-\pi, \pi]$. In such cases, the four-quadrant phase discriminator can maintain stable and correct estimation, avoiding the occurrence of half-cycle slips. In contrast, the two-quadrant phase discriminator yields incorrect phase adjustments, causing the loop to diverge and potentially leading to loss of lock due to error accumulation.

The proposed tracking strategy requires a progressive transition from short to LCI. Initially, a 20 ms integration time is adopted. Once the INS is initialized and aligned, the system tries to enter deep integration mode, wherein dynamic aiding information is employed to control the loop NCO, and the loop bandwidth is subsequently compressed. After the tracking loop is stabilized in deep integration mode, the clock error estimated by the multichannel cooperative tracking loop is applied to eliminate the oscillator instability. At this stage, most of the dynamic stress and clock errors are removed, and the local loop NCO only needs to track the residual errors, enabling LCI. The selection of coherent integration time T_{coh} and loop bandwidth B_n must strictly satisfy the stability constraint to ensure reliable loop behavior, which requires the product of T_{coh} and B_n (NENB) to be less than 0.5 [36], [37]. To further ensure loop stability, a *stepwise integration strategy* is adopted to extend the coherent integration time. Specifically, the coherent integration time is gradually increased in discrete steps. Once the loop maintains stable tracking for a predefined number of epochs at the current integration time, the loop switches to the next longer integration time. This process continues iteratively until the target LCI time is achieved. Throughout this tracking process, if the signal strength falls below a predefined threshold, the loop switches to either the reacquisition mode or the open-loop prediction stage, depending on the loop state.

C. ODO/NHC Distance Increment Measurement Model

The ODO measures the forward distance of a wheeled vehicle by counting wheel encoder pulses. Currently, two primary models are adopted for ODO integration: the distance increment measurement model and the velocity measurement model. The distance increment model directly uses the accumulated travel distance as the measurement, while the velocity model estimates velocity by differentiating distance over time. Based on theoretical modeling and experimental data analysis [33], the ODO distance increment measurement model yields lower measurement error compared to the velocity measurement model, rendering it more suitable for assisting tracking loops under high dynamics and degraded signal conditions. In light of this, the proposed system adopts the distance increment measurement model to mitigate the divergence of INS, particularly during GNSS outages. Additionally, the NHC is incorporated to constrain lateral and vertical motion during calculation, under the assumption that wheeled platforms exhibit negligible displacement in these directions. By jointly applying the forward distance increment from ODO and lateral/vertical constraints from NHC, a 3-D constraint model is constructed.

A Kalman filter is employed to fuse GNSS/INS/ODO measurements for navigation state estimation. The system is formulated within an error-state Kalman Filter (ESKF), where the error state vector is defined as

$$\delta\mathbf{x}_n = \left[(\delta\mathbf{v}^n)^T, (\delta\mathbf{r}^n)^T, \boldsymbol{\varphi}^T, \delta\mathbf{b}_g^T, \delta\mathbf{b}_a^T, \delta\mathbf{k}\right]^T \tag{6}$$

where $\delta\mathbf{r}^n$ denotes the position error of the INS, $\delta\mathbf{v}^n$ is the velocity error, and $\boldsymbol{\varphi}$ represents the attitude error. $\delta\mathbf{b}_g$ and $\delta\mathbf{b}_a$ are the bias errors of the gyroscope and accelerometer, respectively. $\delta\mathbf{k}$ represents the scale factor error of the ODO.

The error state propagation equation is given as

$$\delta\mathbf{x}_n = \boldsymbol{\Phi}_{n/n-1}\delta\mathbf{x}_{n-1} + \boldsymbol{\xi}_{n-1} \tag{7}$$

where $\delta\mathbf{x}_n$ denotes the system error state vector at epoch n, $\boldsymbol{\Phi}_{n/n-1}$ is the error state transition matrix from t_{n-1} to t_n, and $\boldsymbol{\xi}_{n-1}$ represents the process noise during state propagation.

The ODO/NHC velocity measurement equation is given as

$$\mathbf{z}_v = \mathbf{H}_v\delta\mathbf{x}_n + \mathbf{e}_v \tag{8}$$

where $\mathbf{z}_v$ denotes the velocity measurement innovation, $\mathbf{H}_v$ is the velocity measurement matrix, and $\mathbf{e}_v$ represents the velocity measurement error.

Thus, the velocity measurement matrix $\mathbf{H}_v$ can be expressed as

$$\begin{aligned}\mathbf{H}_v = \big[&-\mathbf{K}\mathbf{C}_b^v\left(\left(\mathbf{C}_n^b\mathbf{v}^n\right)\times\right) - \mathbf{K}\mathbf{C}_b^v\left(\mathbf{l}^b\times\right)\left(\left(\mathbf{C}_n^b\boldsymbol{\omega}_{\text{in}}^n\right)\times\right)\\ &- \mathbf{K}\mathbf{C}_b^v\mathbf{C}_n^b, \mathbf{0}_{3\times3}, -\mathbf{K}\mathbf{C}_b^v\left(\mathbf{l}^b\times\right), \mathbf{0}_{3\times3}\\ &- \mathbf{e}_x\mathbf{C}_b^v\left(\mathbf{C}_n^b\mathbf{v}^n + \left(\boldsymbol{\omega}_{nb}^b\times\right)\mathbf{l}^b\right)\big]\end{aligned} \tag{9}$$

where $\mathbf{K} = \text{diag}[1+k\ \ 1\ \ 1]$ is the scale factor matrix of the velocity. $\mathbf{l}^b$ represents the lever arm vector and $\mathbf{e}_x = \text{diag}[1\ 0\ 0]$.

Given the high update rate of the INS, the velocity between two consecutive INS update epochs can be assumed to vary

linearly. Therefore, based on the velocity output from the INS, the estimated distance increments in the three directions of the v-frame from t_{i-1} to t_i can be computed as follows:

$$\Delta\hat{\mathbf{s}}^v = \int_{t_{n-N+1}}^{t_n} \hat{\mathbf{v}}^v \, dt \approx \sum_{i=n-N+1}^{n} \frac{1}{2}\left(\hat{\mathbf{v}}_{i-1}^v + \hat{\mathbf{v}}_i^v\right)\Delta t_i \tag{10}$$

where $\hat{\mathbf{v}}_i^v$ denotes the velocity estimate computed from INS at epoch i and Δt_i represents the time interval between two consecutive epochs.

The velocity measurement model derives the velocity measurement by differentiating the distance increment over time. However, the distance increment measurement model employs the raw distance increment as measurement directly, thereby reducing the impact of quantization noise and avoiding the amplification of high-frequency errors introduced by differentiation. The ODO/NHC distance increment measurement $\Delta\tilde{\mathbf{s}}^v$ can be calculated as

$$\Delta\tilde{\mathbf{s}}^v = \left[\Delta\tilde{s}_{\text{odo}} \; 0 \; 0\right]^T \tag{11}$$

where $\Delta\tilde{s}_{\text{odo}}$ denotes the distance increment measurement of the ODO in the forward direction.

The measurement equation of the ODO/NHC distance increment measurement model is given as

$$\begin{aligned}\mathbf{z}_s &= \Delta\hat{\mathbf{s}}^v - \Delta\tilde{\mathbf{s}}^v = \sum_{i=n-N+1}^{n} \delta\Delta\mathbf{s}_i^v + \mathbf{e}_s \\ &= \frac{1}{2}\sum_{i=n-N+1}^{n}\left(\hat{\mathbf{v}}_{i-1}^v - \mathbf{v}_{i-1}^v + \hat{\mathbf{v}}_i^v - \mathbf{v}_i^v\right)\Delta t_i + \mathbf{e}_s\end{aligned} \tag{12}$$

where $\delta\Delta\mathbf{s}_i^v$ denotes the estimated distance increment error from t_{i-1} to t_i, $\mathbf{v}_i^v$ is the truth vehicle velocity in the v-frame at epoch i, and $\mathbf{e}_s$ is the ODO/NHC distance increment measurement error.

According to the above equations, the measurement matrix of the ODO distance increment measurement model can be derived as

$$\begin{aligned}\mathbf{H}_s = &\frac{1}{2}\mathbf{H}_{v,n-N}\Delta t_{n-N+1}\boldsymbol{\Phi}_{n/n-N}^{-1} \\ &+ \sum_{i=n-N+1}^{n}\mathbf{H}_{v,i}\boldsymbol{\Phi}_{n/i}^{-1}\Delta t_i - \frac{1}{2}\mathbf{H}_{v,n}\Delta t_n\end{aligned} \tag{13}$$

where the state transition matrix $\boldsymbol{\Phi}_{n/i}$ is calculated as follows:

$$\boldsymbol{\Phi}_{n/i} = \boldsymbol{\Phi}_{n/n-1}\cdots\boldsymbol{\Phi}_{i+1/i}. \tag{14}$$

The measurement matrix is derived and used in the ODO/NHC distance increment measurement model. This enables the correction of the accumulated INS errors within each update interval, effectively constraining drift in both the forward and nonholonomic directions and improving the overall dead reckoning robustness.

D. Loop-Aiding Doppler Generation and Accuracy Analysis

To mitigate the dynamic stress imposed on the tracking loop, the Doppler induced by satellite–receiver relative motion is estimated and fed into the carrier phase NCO. Therefore, the tracking loop can handle only residual dynamic errors, enabling longer coherent integration time and supporting further bandwidth compression.

In this process, the navigation states of the vehicle, such as position, velocity, and acceleration, are propagated by INS, while GNSS and ODO measurements are used to periodically update the Kalman Filter, correcting the INS errors. The satellites' positions and velocities are derived from the broadcast ephemeris during RTK processing. Afterward, the relative motion between the satellite and receiver is computed, and the corresponding Doppler is derived and injected into the tracking loop to compensate for the dynamic stress.

The loop-aiding Doppler is denoted as

$$f_{\text{Aid}} = f_R + f_S^{(i)} = \mathbf{I}_{\text{Los}}^{(i),e}\left(-\frac{\mathbf{v}_{RS^{(i)}}}{\lambda}\right) \tag{15}$$

where f_R and $f_S^{(i)}$ represent the Doppler caused by the motion of the receiver and the ith satellite, respectively. $\mathbf{I}_{Los}^{(i),e}$ is the unit line-of-sight (LOS) vector between the receiver and the ith satellite. $\mathbf{v}_{RS^{(i)}}$ represents the relative velocity between the receiver and the ith satellite. And λ is the wavelength of the satellite signal. The LOS unit vector $\mathbf{I}_{\text{Los}}^{(i),e}$ is derived based on the relative positions of the satellite and the receiver

$$\mathbf{I}_{\text{Los}}^{(i),e} = \frac{\mathbf{P}_S^{(i),e} - \mathbf{P}_R^e}{\left\|\mathbf{P}_S^{(i),e} - \mathbf{P}_R^e\right\|} \tag{16}$$

where $\mathbf{P}_S^{(i),e}$ and $\mathbf{P}_R^e$ denote the position of the ith satellite and the receiver in the Earth-centered Earth-fixed (ECEF) frame, respectively.

To promptly compensate for the dynamic stress in the tracking loop, the update rate of the loop-aiding Doppler must be sufficiently high. To achieve a high-rate output of loop-aiding Doppler, it is necessary to apply a linear extrapolation to the Doppler information of both the receiver and the satellite. In terms of the Doppler caused by the receiver motion, a constant-acceleration linear extrapolation model is applied as follows:

$$f_R\left(nT_I + \Delta t\right) = f_R\left(nT_I\right) - \frac{\Delta t}{\lambda}\mathbf{I}_{\text{Los}}^{(i),e}\cdot\mathbf{a}_R\left(nT_I\right) \tag{17}$$

where T_I denotes the IMU update interval, n is the index of the current update epoch, Δt represents the time offset between the extrapolation moment and the previous update epoch, and $\mathbf{a}_R(nT_I)$ is the acceleration estimated at the current epoch based on the INS propagation.

Similarly, a constant-acceleration linear extrapolation model is applied to the Doppler caused by the satellite motion. Assuming that the Doppler of the satellite varies linearly within the update interval, the Doppler value at the extrapolation time can be predicted by using the time derivative of Doppler between two adjacent epochs

$$\begin{aligned}f_s\left(nT_R + \Delta t\right) = &f_s\left(nT_R\right) \\ &+ \frac{f_s\left(nT_R\right) - f_s\left(\left(n-1\right)T_R\right)}{T_R}\cdot\Delta t\end{aligned} \tag{18}$$

where T_R represents the update interval of the RTK processing, which is typically 1 s. The linear extrapolation is based on the assumption that both the receiver and the satellites' motion follow the constant acceleration model between two consecutive update epochs. In addition, the change in the LOS vector due to motion is assumed to be negligible.

To elucidate the impacts of different types of multisensor aiding information on the tracking loop, we analyze the aiding

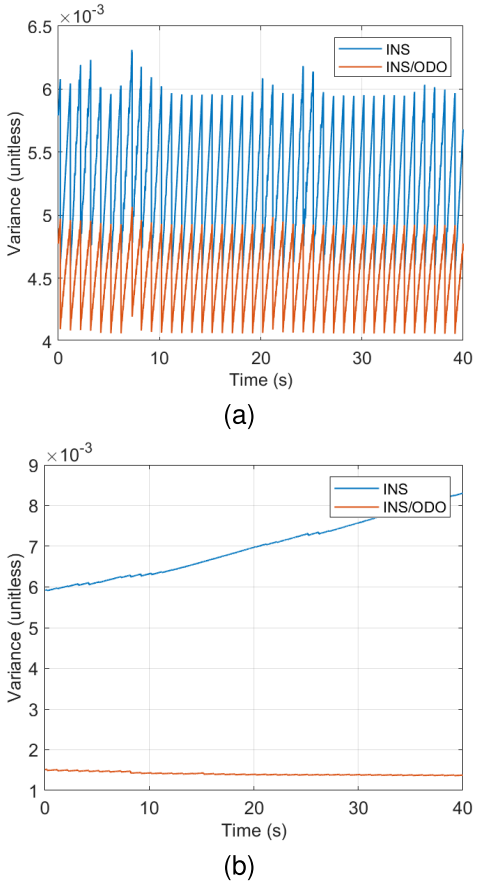

Fig. 4. Variance of system error states with different sensor fusion. (a) Variance of δv_N from the P matrix. (b) Variance of φ_y from the P matrix.

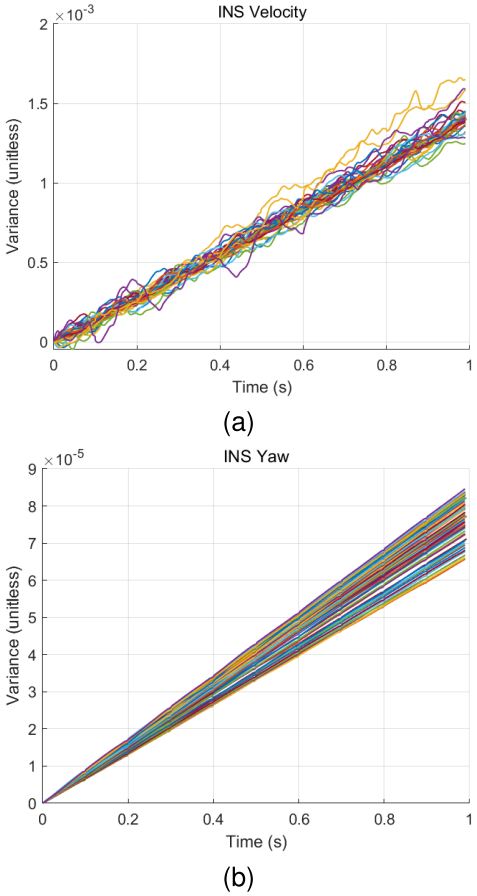

Fig. 5. Variance of system error states of the MEMS IMU over 1 s. (a) Variance of δv_N. (b) Variance of φ_y.

performance of a standalone MEMS IMU and that of a MEMS IMU/ODO integration on the carrier phase tracking loop. During the coherent integration accumulation stage, only the aiding information is used to control the loop NCO. As a result, the local loop can be regarded as operating in an open-loop mode in this case. The local tracking errors are completely determined by the aiding Doppler error. According to (15), the Doppler aiding error can be expressed

$$\delta f_{\text{Aid}}(s) = \frac{\delta \mathbf{v}_{\text{Aid}}(s)}{\lambda} \mathbf{I}_{\text{Los}}^{(i),e} \tag{19}$$

where $\delta \mathbf{v}_{\text{Aid}}(s)$ denotes the velocity error during a coherent integration interval.

According to [23], [38], the initial velocity and attitude errors are the dominant factors influencing the performance of deep integration tracking loops. Therefore, this study focuses on analyzing the velocity and attitude errors of standalone INS and INS/ODO systems, which determine the effectiveness of dynamic stress compensation during the LCI accumulation process. As the INS/ODO integration is highly nonlinear, a simulation test was conducted. We used experimental data collected along a north–south trajectory in an open-sky environment and compared the covariance matrix (P) of the system error states estimated by the ESKF under different sensor integration schemes. Fig. 4 shows the variance of the north velocity and heading errors of a GNSS/INS and a GNSS/INS/ODO system, respectively, over a 40-s interval. As shown in the figure, the errors grow rapidly in the GNSS/INS system because the navigation relies solely on INS propagation during two GNSS update epochs. The integration of the INS and the ODO distance increment measurement can suppress the divergence of velocity and heading errors.

To further investigate the impact of different aiding information on the extension of coherent integration time, we analyzed the divergence characteristics of the error state variance at a 1-s interval under different sensor fusion schemes. Assuming that the GNSS corrections are accurate, the variance of the error states is set to zero. Based on the results in Fig. 4, 60 1-s samples were selected, and the corresponding results are plotted in Figs. 5 and 6. In the absence of external corrections, the standalone INS exhibits rapid error divergence in both velocity and heading, whereas the ODO's distance increment measurement provides significant corrections to the INS, thereby mitigating the error divergence. Since the ODO distance increment measurement relies on the distance in the forward direction, which is relatively stable, each correction maintains a fairly consistent magnitude.

Moreover, in our previous study [33], we compared the ODO distance increment measurement model with the conventional velocity measurement model. It was derived that the distance increment measurement error decreases by approximately 72% compared with the velocity measurement error. By modeling the lateral and vertical speed errors as random white noise, the theoretical error decrease of the lateral and vertical distance increment is 93%. These results confirm

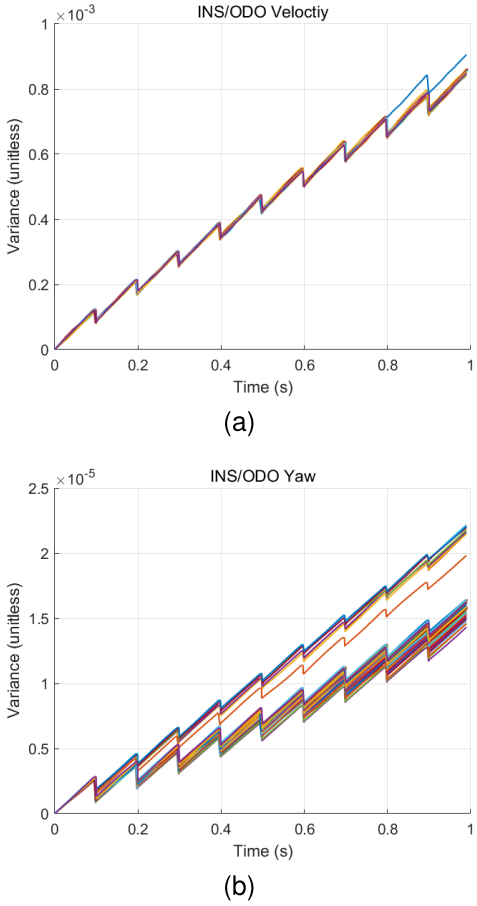

Fig. 6. Variance of system error states of INS/ODO over 1 s. (a) Variance of δv_N. (b) Variance of φ_y.

Fig. 7. Snapshot of experimental scenarios.

that the distance increment formulation effectively suppresses measurement noise and improves Doppler prediction accuracy.

Based on the above results and analysis, it is evident that the MEMS IMU/ODO distance increment measurement model integrated system introduces smaller velocity and attitude errors, thereby providing more accurate aiding Doppler to mitigate the dynamic stress during coherent integration.

III. Experimental Setup

To evaluate the performance of the proposed GIO-DC system, a field experiment was conducted on the campus of Wuhan University. The experimental environment, as illustrated in Fig. 7, includes dense foliage canopies and building obstructions. The tree canopies and trunks result in attenuation and frequent blockage of satellite signals. The building

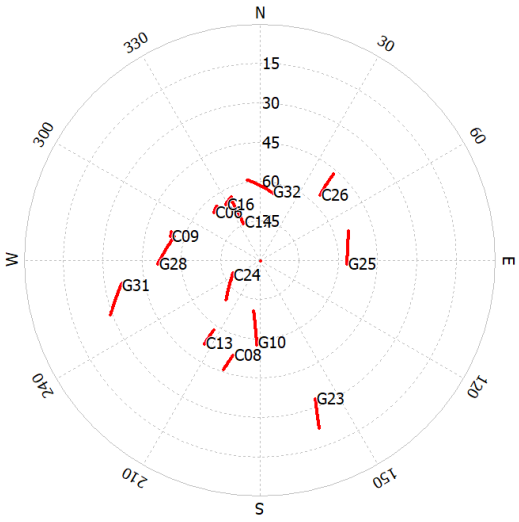

Fig. 8. Distribution of satellites.

obstructions lead to severe multipath effects and signal degradation. Such challenging scenarios serve as a comprehensive and realistic testbed to validate the carrier phase tracking accuracy and robustness of the GIO-DC system.

The experimental data were collected using a wheeled robotic platform equipped with a variety of navigation sensors. The satellite signals received by the antenna were distributed via a power splitter to different devices. A Spirent GNSS signal record and playback system GSS6450 [39] was used to record the RF signals and downconvert them to IF signals. The IF signals were subsequently processed by a software-defined GNSS receiver. Fig. 8 shows the satellite distribution during the experiment. Only GPS and BDS L1 signals were utilized. A high-precision positioning and orientation system (POS), the Leador A15, integrating a multifrequency and multiconstellation GNSS receiver and a navigation-grade IMU, was used to provide postprocessed navigation results as the reference ground truth for evaluation. Additionally, a geodetic GNSS receiver, the NoVatel 718D, was employed to collect satellite signals for comparative analysis. The platform was also equipped with a low-cost MEMS IMU (ICM20602) and an ODO mounted on the wheeled robot. The IMU and ODO are both sampled at 200 Hz. The ODO wheel has a diameter of 0.147 m and a resolution of 800 pulses per revolution. All sensor data were synchronized to GPS time.

The static base station used in the experiment was deployed on a rooftop under an open-sky environment to provide high-quality reference data. A geodetic GNSS receiver, the Panda, was used to collect base station observations, which were subsequently utilized for RTK positioning processing. The software-defined GNSS/INS/ODO deeply integrated receiver I2xSNR, developed by the I2Nav team, was employed to process the data of the ICM20602, ODO, and GSS6450. The performance of the GIO-DC system will be evaluated across multiple levels. The key parameters of the reference navigation-grade IMU (Leador A15) and the tested MEMS IMU (ICM20602) are summarized in Table I.

IV. Results and Discussion

This section presents dynamic test results of the GIO-DC system in typical challenging scenarios with dense foliage

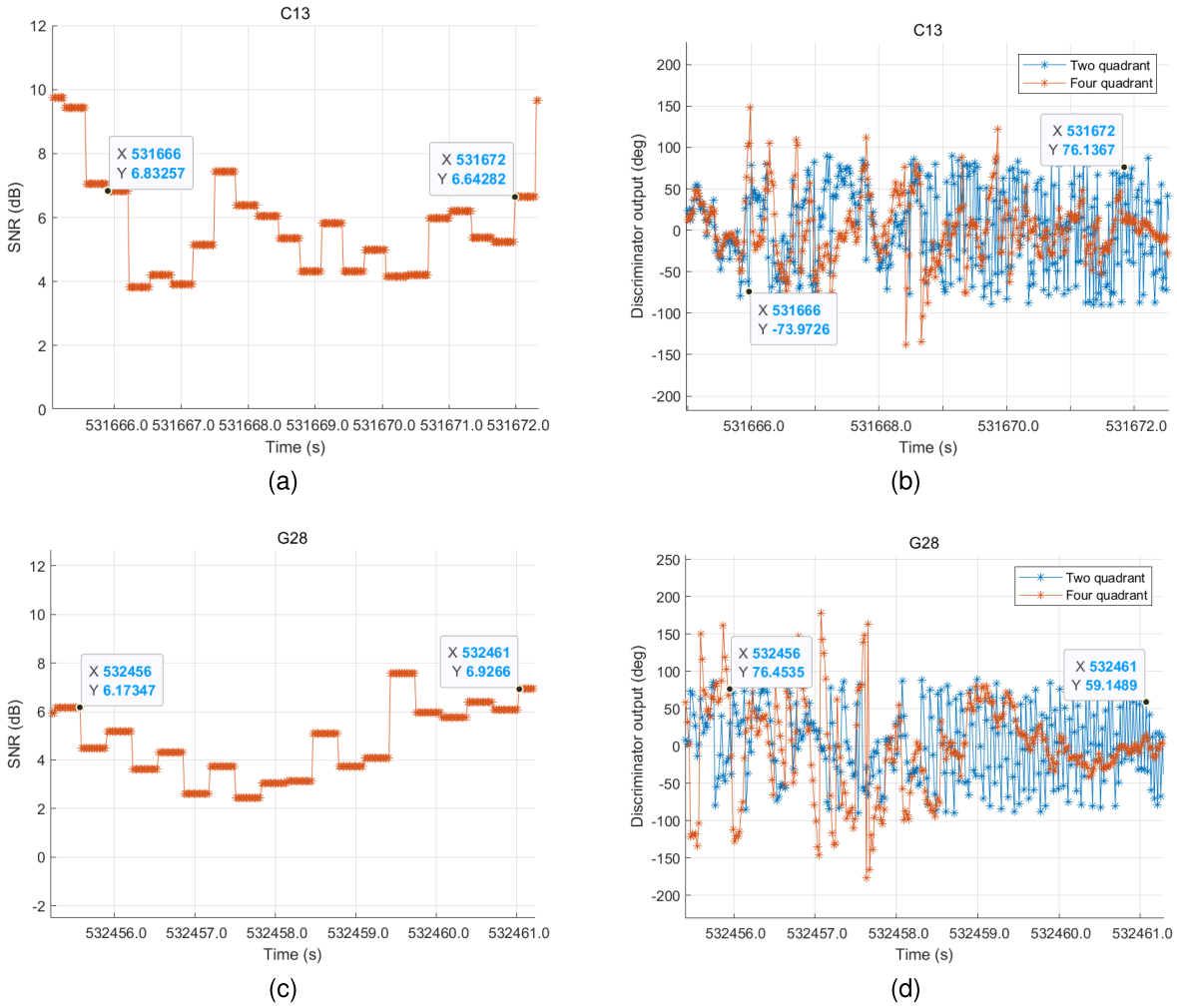

Fig. 9. Comparison of the two- and four-quadrant phase discriminators. (a) SNR of BDS13. (b) Discriminator output of BDS13. (c) SNR of GPS28. (d) Discriminator output of GPS28.

TABLE I
PARAMETERS OF TESTING IMUS

Parameter	Leador A15	ICM20602
Gyro bias instability (deg/hr)	0.027	50
Gyro random walk (deg/$\sqrt{\text{hr}}$)	0.003	0.24
Accel bias instability (mGal)	15	250
Accel random walk (m/s/$\sqrt{\text{hr}}$)	0.03	0.24

canopies and building obstructions. The evaluation includes: the performance assessment of the carrier phase discriminator, the impact of INS/ODO assistance on LCI performance, the influence of different LCI times, the carrier phase observations, and the positioning performance of the proposed system.

A. Four-Quadrant Phase Discriminator Performance Analysis

The four-quadrant phase discriminator is introduced to extend the phase error detection range and reduce the risk of losing lock in complex environments. This test will compare the performance of the two-quadrant and four-quadrant phase discriminators in challenging environments.

Fig. 9 presents the outputs of the two types of discriminators of BDS13 and GPS8 using the GIO-DC system configured with a 20-ms coherent integration time and a 3-Hz loop bandwidth. The estimation of the SNR is based on an FFT operation that calculates the ratio between the signal and noise components in the frequency domain. More details can be found in [40].

In Fig. 9(a) and (b), during the interval from 531 666 to 531 672 s, the SNR of BDS13 dropped below 6 dB, resulting in a temporary loss of lock when using the two-quadrant phase discriminator. In contrast, the four-quadrant phase discriminator exhibited a significant phase error of approximately 150° during this low-SNR period, which did not exceed its pull-in range, enabling continuous carrier phase tracking.

In Fig. 9(c) and (d), a more challenging scenario occurred between 532 456 and 532 461 s, where the SNR further degraded to 6 dB or even below 3 dB. While the four-quadrant phase discriminator experienced several large instantaneous phase discrimination errors, it was still able to maintain continuous tracking. As the SNR subsequently improved, the discriminator rapidly returned to accurate and stable tracking.

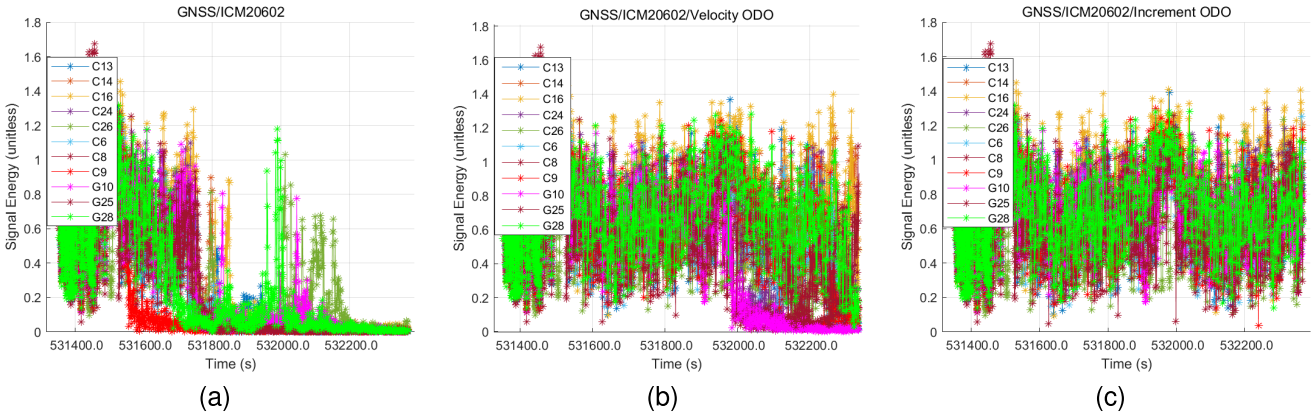

Fig. 10. Signal energy of different aiding methods. (a) Energy in the ICM20602-aided loop. (b) Energy in the IMU/ODO velocity model-aided loop. (c) Energy in the IMU/ODO distance increment model-aided loop.

In contrast, the two-quadrant phase discriminator completely lost lock during this period and failed to recover within the interval.

The comparison demonstrates that the four-quadrant phase discriminator is obviously superior to the two-quadrant phase discriminator in complex environments. It can avoid the loss of lock caused by the phase errors falling into $[-\pi, -\pi/2]$ and $[\pi/2, \pi]$. This enhanced stability allows for more stable loop tracking and supports the consistent output of carrier phase observations for high-precision positioning.

B. ODO/NHC Distance Increment Measurement Model Performance Analysis

In this test, the primary objective is to evaluate the influence of different ODO implementation strategies on the performance of the LCI tracking loop. The inertial sensor used in this study is a low-cost MEMS IMU (ICM20602), representing a typical consumer-grade sensor configuration in cost-sensitive applications.

As mentioned before, as the coherent integration time extends, the loop is more sensitive to the dynamic stress. To thoroughly evaluate the influence of different aiding strategies on the performance of LCI tracking, the GIO-DC system was tested under an integration period of 1 s. This extreme configuration amplifies the dependence on precise dynamic assistance and serves as a robust benchmark for assessing the effectiveness of various aiding methods.

The energy of a predetection signal after coherent integration is defined as

$$E = I^2 + Q^2 \tag{20}$$

where I and Q represent the in-phase and quadrature components of the signal output after coherent integration, respectively.

To facilitate quantitative analysis, the normalized energy is used to express the signal strength [25]. First, a reference energy is established by selecting up to N epochs in which the PLI exceeds a predefined threshold, indicating stable signal tracking. The mean energy over these N epochs is taken as the reference energy, establishing an energy benchmark under a specific loop configuration. The dimensionless normalized energy is then defined as the ratio between the instantaneous energy and the reference energy

$$E_{\text{norm}} = \frac{E}{E_{\text{ref}}} \tag{21}$$

where E_{ref} is the reference energy established from the stable tracking epochs.

The normalized energy serves as an indicator of the relative signal strength with respect to the energy observed under stable tracking conditions. Higher normalized energy values indicate stronger signal stability and more reliable tracking performance. Conversely, a notable decline in normalized energy typically reflects the occurrence of interference within the tracking loop.

Fig. 10 shows the normalized energy output of different satellites with a 1-s coherent integration period. Three different strategies are compared: the stand-alone ICM20605 IMU assistance, IMU/ODO assistance using the velocity measurement model, and IMU/ODO assistance using the distance increment measurement model.

The 1-s coherent integration loop operates with an ultra-narrow bandwidth of 0.2 Hz, making it highly sensitive to the dynamic residuals after deeply coupled integration is applied. When the stand-alone IMU assistance is adopted, the normalized energy of all satellites drops to nearly zero after 531 600 s, indicating a complete loss of lock on all channels [Fig. 10(a)]. When IMU/ODO assistance based on the velocity measurement model is adopted, only a limited number of channels can maintain stable tracking of the carrier phase signals throughout the whole experiment, and the other channels lose lock [Fig. 10(b)]. This is because the IMU/ODO assistance based on the velocity measurement model cannot fully compensate for dynamic stress, resulting in large dynamic residuals that must be tracked by the LCI loop. In this case, even a minor extra interference can cause the loop to lose lock. In contrast, when the IMU/ODO assistance based on the distance increment measurement model is adopted, all channels achieve continuous and stable satellite signal tracking [Fig. 10(c)]. This performance improvement is attributed to the fact that the IMU/ODO integration based on the distance increment measurement model can provide more accurate loop-aiding information. As discussed in the ODO/NHC Distance Increment Measurement Model section,

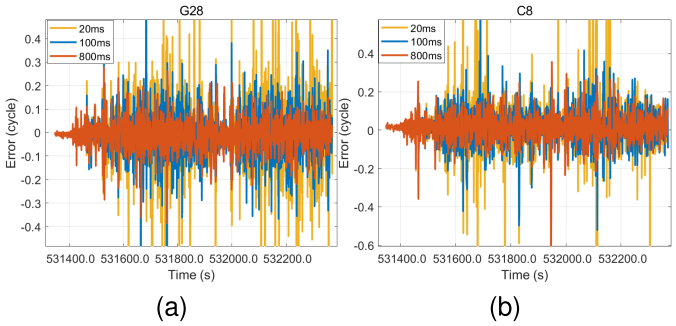

Fig. 11. Carrier phase observation errors of the GIO-DC system under different integration periods. (a) Carrier phase observation errors of GPS28. (b) Carrier phase observation errors of BDS8.

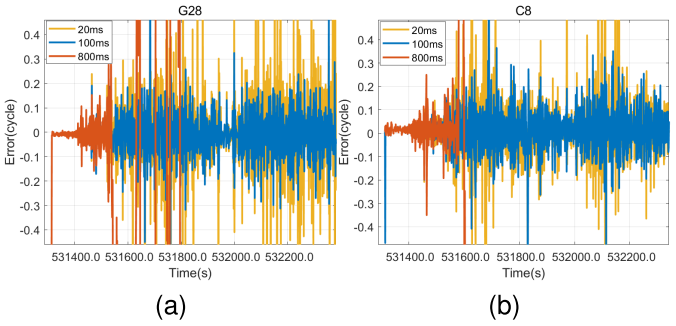

Fig. 12. Carrier phase observation errors of the ICM20602-aided deep integration system under different integration periods. (a) Carrier phase observation errors of GPS28. (b) Carrier phase observation errors of BDS8.

the distance increment measurement model introduces lower measurement errors than the velocity model, making it more effective in mitigating dynamic stress within the tracking loop and enabling longer coherent integration time. As a result, the distance increment measurement model is adopted in the GIO-DC system for the subsequent tests.

C. Effect of Integration Times on Tracking Performance

In Section IV-B, an ultralong integration period of 1 s was used, representing an extreme experimental condition for evaluating the accuracy of the aiding information. However, the settings of the integration time and loop bandwidth face a tradeoff between the residual dynamic response and thermal noise mitigation. On one hand, the coherent integration time should be as long as possible to maximize its effectiveness in weak signal tracking and multipath mitigation. On the other hand, excessively long LCI time increases the loop's vulnerability to residual dynamic stress and aiding errors, potentially leading to tracking degradation or loss of lock. Considering this tradeoff, an integration time of up to 800 ms is adopted in practical applications. In this subsection, the observation errors of both the GIO-DC system and the ICM20602-aided deep integration system are compared under different coherent integration periods (20, 100, and 800 ms) to evaluate their practical effectiveness in supporting LCI. The carrier observation errors are derived using the GNSS triple-difference method.

Fig. 11 presents the carrier phase observation errors of GPS28 and BDS8 with coherent integration periods/loop bandwidths of 20 ms/3 Hz, 100 ms/1 Hz, and 800 ms/0.3 Hz. It is evident that increasing the integration time leads to a reduction in carrier phase observation errors. Compared to the 20-ms coherent integration period, the occurrence of cycle slips is significantly reduced under both the 100- and 800-ms settings. It is noteworthy that while a few cycle slips remain when the coherent integration time is 100 ms, they are nearly eliminated under the 800-ms configuration.

Fig. 12 shows the carrier phase observation errors of GPS28 and BDS8 using the ICM20602-aided deep integration system under the same coherent integration periods. It can be observed that the carrier phase observation errors are significantly reduced when the coherent integration time increases from 20 to 100 ms. However, when the coherent integration period is further extended to 800 ms, most satellites lose lock, resulting in either missing carrier phase observations or large outliers. This indicates that the pure MEMS IMU-aided deep integration system is constrained by the accuracy of MEMS IMU aiding, limiting its ability to support 800-ms coherent integration. Therefore, the following analysis focuses on the observation errors of the GIO-DC system under different coherent integration periods to further evaluate its robustness and LCI performance.

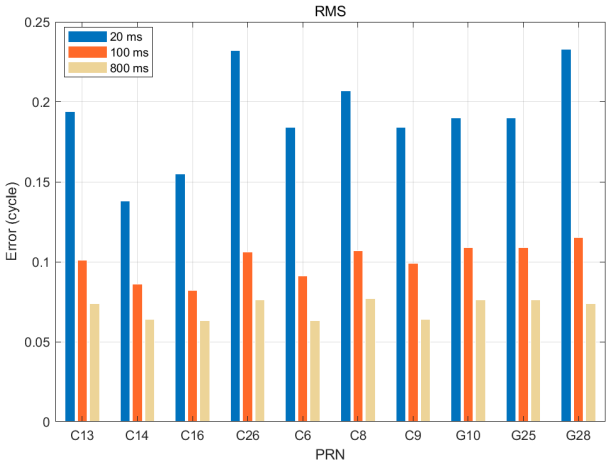

Fig. 13. RMS of different integration periods.

Fig. 13 presents the rms of the carrier phase observation errors of the GIO-DC system under three different coherent integration periods. The results demonstrate that as the integration period increases, the rms error of the carrier phase observations progressively decreases. Notably, the 800-ms integration period achieves an rms error below 0.1 cycle. Longer coherent integration time improves the SNR significantly and leads to better discrimination of error signals, thereby enabling more stable signal tracking in challenging environments. The results presented in this subsection validate the effectiveness of the GIO-DC system in supporting LCI, thereby enhancing the accuracy of carrier phase observations and reducing the occurrence of cycle slips. The 800-ms coherent integration time and 0.3-Hz loop bandwidth present the best overall performance, which will be used in the subsequent performance evaluation.

D. Carrier Phase Observation and Positioning Performance Evaluation

In this section, the overall performance of the proposed GIO-DC system is evaluated. The use of a four-quadrant phase discriminator extends the pull-in range of the LCI

TABLE II
CARRIER PHASE OBSERVATION ERROR STATISTICS OF DIFFERENT SOLUTIONS

PRN	Solution	RMS (cycle)	CEP95 (cycle)	Valid Epochs (%)
C13	NoVatel 718D	0.440	0.307	81.6
	GIO-DC 800 ms	**0.074**	**0.115**	**99.8**
	GNSS/Leador A15 800 ms	0.067	0.114	99.8
C14	NoVatel 718D	0.302	0.178	95.5
	GIO-DC 800 ms	**0.064**	**0.099**	**100**
	GNSS/Leador A15 800 ms	0.061	0.094	100
C16	NoVatel 718D	0.256	0.196	91.0
	GIO-DC 800 ms	**0.063**	**0.100**	**99.8**
	GNSS/Leador A15 800 ms	0.060	0.097	99.8
C26	NoVatel 718D	0.385	0.275	80.3
	GIO-DC 800 ms	**0.076**	**0.109**	**100**
	GNSS/Leador A15 800 ms	0.072	0.109	100
C6	NoVatel 718D	0.332	0.210	89.6
	GIO-DC 800 ms	**0.063**	**0.103**	**100**
	GNSS/Leador A15 800 ms	0.060	0.097	100
C8	NoVatel 718D	0.428	0.272	74.8
	GIO-DC 800 ms	**0.077**	**0.123**	**98.6**
	GNSS/Leador A15 800 ms	0.070	0.125	98.6
C9	NoVatel 718D	0.368	0.219	84.7
	GIO-DC 800 ms	**0.064**	**0.109**	**99.8**
	GNSS/Leador A15 800 ms	0.059	0.100	99.8
G10	NoVatel 718D	0.395	0.330	89.9
	GIO-DC 800 ms	**0.076**	**0.117**	**100**
	GNSS/Leador A15 800 ms	0.074	0.111	100
G25	NoVatel 718D	0.110	0.200	82.6
	GIO-DC 800 ms	**0.074**	**0.123**	**99.8**
	GNSS/Leador A15 800 ms	0.071	0.115	99.8
G28	NoVatel 718D	0.110	0.191	75.9
	GIO-DC 800 ms	**0.072**	**0.106**	**99.8**
	GNSS/Leador A15 800 ms	0.065	0.095	99.9

tracking loop. This significantly reduces the likelihood of losing lock in complex environments. Integrating the ODO distance increment measurement with the MEMS IMU provides more accurate dynamic aiding information. This effectively mitigates most of the dynamic stress within the tracking loop.

To validate the effectiveness of the system, we compare three solutions: 1) the geodetic GNSS receiver (NovAtel 718D); 2) the GIO-DC system with an 800 ms coherent integration time; and 3) the deeply integrated GNSS/navigation-grade IMU (Leador A15) system with the same integration time.

Table II summarizes the rms error, 95% circular error probable (CEP95), and the proportion of valid epochs of GNSS carrier phase observations across various positioning solutions. A five-cycle carrier phase error corresponds to approximately 1 m in positioning error. In high-precision GNSS applications, such an error is considered a large gross error. Therefore, the observation errors of less than five cycles are regarded as valid epochs. As shown in Table II, compared with the standalone geodetic GNSS receiver, the deeply integrated system substantially reduces carrier phase observation errors for all satellites. Compared with the reference NovAtel 718D system, the proposed GIO-DC system reduces rms and CEP95 errors by 70.7% and 51.6%, respectively, averaged over all satellites. It also significantly increases the proportion of valid epochs. Moreover, the results indicate that the GIO-DC system achieves a GNSS carrier phase measurement accuracy comparable to that of the navigation-grade IMU-based deeply integrated system. This confirms the effectiveness of low-cost MEMS IMU/ODO assistance in enhancing the continuity and reliability of carrier phase observations in complex environments.

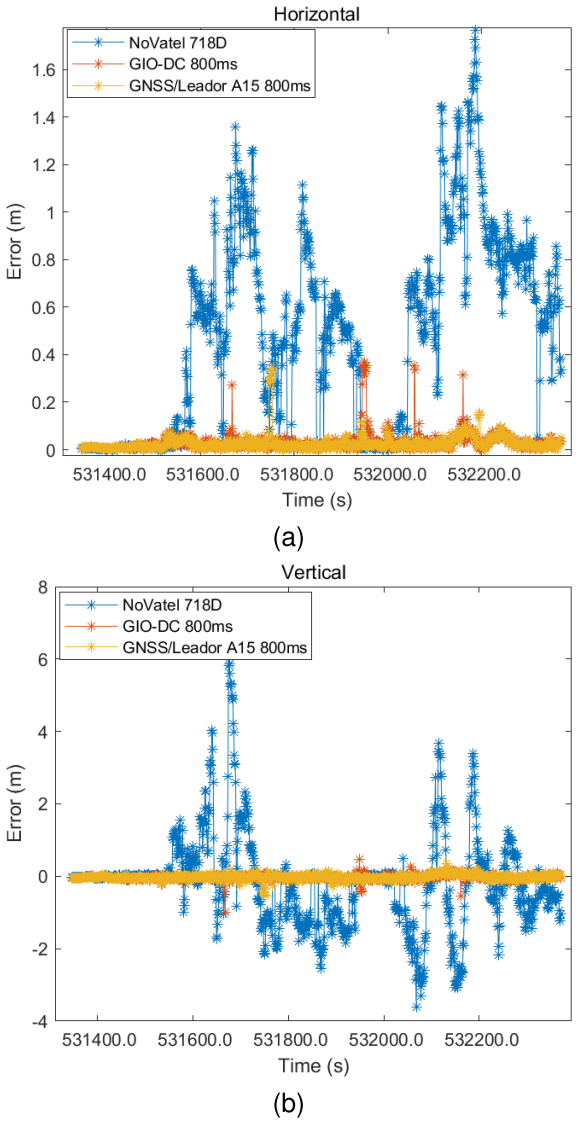

Fig. 14. Positioning errors of different solutions. (a) Horizontal positioning errors. (b) Vertical positioning errors.

We employ a common RTK positioning algorithm, PLANSoft, developed by the Position, Location and Navigation (PLAN) team at the University of Calgary [41], to process the observations from the above configurations. The positioning performance of the three solutions is analyzed, and the corresponding positioning errors in both horizontal and vertical directions are shown in Fig. 14. The NovAtel 718D positioning solution exhibits many instances of both nonfixed and fixed errors, whereas the GIO-DC and the GNSS/navigation-grade IMU deeply integrated systems show only a few cases of fixed errors.

In the horizontal direction, the CEP95 errors of the NovAtel 718D, the GIO-DC system, and the deeply integrated GNSS/navigation-grade IMU system are 1.170, 0.074, and 0.069 m, respectively. The corresponding CEP68 errors are 0.676 0.030, and 0.026 m. Both the GIO-DC system and the GNSS/navigation-grade IMU deeply integrated system achieve centimeter-level positioning accuracy. The positioning

error comparison further demonstrates that MEMS IMU/ODO assistance can achieve dynamic stress mitigation performance comparable to that of a standalone navigation-grade IMU. This enables significantly extended coherent integration times and supports reliable high-precision positioning in complex environments.

V. Conclusion

We propose a GIO-DC system that leverages a MEMS IMU and an ODO to assist the PLLs, realizing effective LCI carrier phase signal tracking. The ODO/NHC distance increment measurement model produces lower velocity errors compared to the traditional velocity measurement model, enabling to provide more accurate dynamic aiding information. By combining a low-cost consumer-grade MEMS IMU (ICM20602) with the ODO/NHC distance increment measurement model, the system effectively estimates and compensates for the dynamic stress arising from satellite–receiver relative motion, thus enabling a substantial extension of coherent integration time. Moreover, a four-quadrant phase discriminator is employed to extend the pull-in range of the tracking loop, significantly enhancing the robustness of the LCI carrier phase tracking architecture.

To validate the performance of the proposed system, a series of experimental tests was conducted. The proposed GIO-DC system is capable of achieving a coherent integration time up to the 1 s limit even under challenging conditions. Under an optimized configuration with an 800 ms coherent integration time and a 0.3 Hz PLL bandwidth, the system achieves carrier phase tracking and positioning performance comparable to that of a navigation-grade IMU-based solution, enabling centimeter-level accuracy in complex environments. These results confirm the effectiveness of fusing a consumer-grade MEMS IMU with an ODO/NHC distance increment measurement model in facilitating LCI.

In practical applications, the proposed system shows strong potential for autonomous driving, precision farming, and urban navigation. The improved tracking robustness and positioning accuracy of the GIO-DC architecture enable reliable navigation even in GNSS-challenged environments such as urban canyons and areas with severe multipath interference. In future work, additional sensors such as LiDAR may be integrated into the deeply coupled architecture to further improve the performance of LCI tracking loops and enhance robustness against multipath effects in challenging environments.

References

[1] Y. V. Yasyukevich, B. Zhang, and V. R. Devanaboyina, "Advances in GNSS positioning and GNSS remote sensing," *Sensors*, vol. 24, no. 4, p. 1200, Feb. 2024.

[2] L. Chen, F. Zheng, X. Gong, and X. Jiang, "GNSS high-precision augmentation for autonomous vehicles: Requirements, solution, and technical challenges," *Remote Sens.*, vol. 15, no. 6, p. 1623, Mar. 2023.

[3] N. Joubert, T. G. R. Reid, and F. Noble, "Developments in modern GNSS and its impact on autonomous vehicle architectures," in *Proc. IEEE Intell. Vehicles Symp. (IV)*, Oct. 2020, pp. 2029–2036.

[4] E. Schmidt, D. Akopian, and D. J. Pack, "Development of a real-time software-defined GPS receiver in a LabVIEW-based instrumentation environment," *IEEE Trans. Instrum. Meas.*, vol. 67, no. 9, pp. 2082–2096, Sep. 2018.

[5] N. Zhu, J. Marais, D. Bétaille, and M. Berbineau, "GNSS position integrity in urban environments: A review of literature," *IEEE Trans. Intell. Transp. Syst.*, vol. 19, no. 9, pp. 2762–2778, Sep. 2018.

[6] T. Pany et al., "Coherent integration time: The longer, the better," *Inside GNSS*, vol. 4, pp. 52–61, Nov. 2009.

[7] X. Feng, T. Zhang, X. Niu, T. Pany, and J. Liu, "Improving GNSS carrier phase tracking using a long coherent integration architecture," *GPS Solutions*, vol. 27, no. 1, p. 37, Jan. 2023.

[8] C. O'Driscoll, M. G. Petovello, and G. Lachapelle, "Choosing the coherent integration time for Kalman filter-based carrier-phase tracking of GNSS signals," *GPS Solutions*, vol. 15, no. 4, pp. 345–356, Oct. 2011.

[9] P. Xie and M. G. Petovello, "Measuring GNSS multipath distributions in urban canyon environments," *IEEE Trans. Instrum. Meas.*, vol. 64, no. 2, pp. 366–377, Feb. 2015.

[10] T. Pany, H. Euler, and J. Winkel, "Indoor carrier phase tracking and positioning with difference correlators," in *Proc. 24th Int. Tech. Meeting Satell. Division Inst. Navigat. (ION GNSS)*, 2011, pp. 2202–2213.

[11] S. Chen, Y. Gao, and T. Lin, "Effect and mitigation of oscillator vibration-induced phase noise on carrier phase tracking," *GPS Solutions*, vol. 21, no. 4, pp. 1515–1524, Oct. 2017.

[12] R. Yang, Y. Morton, K.-V. Ling, and E.-K. Poh, "Generalized GNSS signal carrier tracking—Part II: Optimization and implementation," *IEEE Trans. Aerosp. Electron. Syst.*, vol. 53, no. 4, pp. 1798–1811, Aug. 2017.

[13] K.-W. Chiang and Y.-W. Huang, "An intelligent navigator for seamless INS/GPS integrated land vehicle navigation applications," *Appl. Soft Comput.*, vol. 8, no. 1, pp. 722–733, Jan. 2008.

[14] E. V. Hinüber, C. Reimer, T. Schneider, and M. Stock, "INS/GNSS integration for aerobatic flight applications and aircraft motion surveying," *Sensors*, vol. 17, no. 5, p. 941, Apr. 2017.

[15] P. Ye, X. Zhan, and C. Fan, "Novel optimal bandwidth design in INS-assisted GNSS phase lock loop," *IEICE Electron. Exp.*, vol. 8, no. 9, pp. 650–656, 2011.

[16] F. Qin, X. Zhan, and G. Du, "Performance improvement of receivers based on ultra-tight integration in GNSS-challenged environments," *Sensors*, vol. 13, no. 12, pp. 16406–16423, Dec. 2013.

[17] Y. Luo, C. Yu, S. Chen, J. Li, H. Ruan, and N. El-Sheimy, "A novel Doppler rate estimator based on fractional Fourier transform for high-dynamic GNSS signal," *IEEE Access*, vol. 7, pp. 29575–29596, 2019.

[18] Y. Luo, L.-T. Hsu, and N. El-Sheimy, "A baseband MLE for snapshot GNSS receiver using super-long-coherent correlation in a fractional Fourier domain," *Navig., J. Inst. Navigat.*, vol. 70, no. 3, 2023.

[19] Y. Luo, L.-T. Hsu, C. L. Tsang, and N. El-Sheimy, "An unassisted super-resolution satellite navigation receiver using GPS L5 signals," *IEEE Trans. Aerosp. Electron. Syst.*, vol. 59, no. 6, pp. 7666–7680, Dec. 2023.

[20] T. Ren and M. G. Petovello, "A stand-alone approach for high-sensitivity GNSS receivers in signal-challenged environment," *IEEE Trans. Aerosp. Electron. Syst.*, vol. 53, no. 5, pp. 2438–2448, Oct. 2017.

[21] T. Pany et al., "Performance of a partially coherent ultra-tightly coupled GNSS/INS pedestrian navigation system enabling coherent integration times of several seconds to track GNSS signals down to 1.5 dBHz," in *Proc. 22nd Int. Tech. Meeting Satell. Division Inst. Navigat. (ION GNSS)*, 2009, pp. 919–934.

[22] Z. Cheng et al., "Real-time multipath mitigation with sensor-aided long coherent integration (SALI)," in *Proc. ION GNSS+, Int. Tech. Meeting Satell. Division Inst. Navigat.*, Oct. 2024, pp. 2615–2629.

[23] X. Niu, Y. Ban, Q. Zhang, T. Zhang, H. Zhang, and J. Liu, "Quantitative analysis to the impacts of IMU quality in GPS/INS deep integration," *Micromachines*, vol. 6, no. 8, pp. 1082–1099, Aug. 2015.

[24] A. Soloviev and T. Jeffrey Dickman, "Deeply integrated GPS for indoor navigation," in *Proc. Int. Conf. Indoor Positioning Indoor Navigat.*, Sep. 2010, pp. 1–9.

[25] T. Zhang, X. Feng, X. Niu, M. Bochkati, T. Pany, and J. Liu, "GNSS carrier phase improvement using a MEMS INS-aided long coherent architecture for high precision navigation," *IEEE Trans. Intell. Transp. Syst.*, vol. 25, no. 11, pp. 16745–16760, Nov. 2024.

[26] J. Dampf, M. Bochkati, and T. Pany, "Towards single antenna phase-coherent INS-beamforming to enable RTK with low-end antennas," in *Proc. ION GNSS+, Int. Tech. Meeting Satell. Division Inst. Navigat.*, Oct. 2022, pp. 2202–2214.

[27] M. Bochkati, J. Dampf, and T. Pany, "Receiver clock estimation for RTK-grade multi-GNSS multi-frequency synthetic aperture processing," in *Proc. IEEE/ION Position, Location Navigat. Symp. (PLANS)*, Apr. 2023, pp. 968–976.

[28] V. Suvorkin, M. Garcia-Fernandez, G. González-Casado, M. Li, and A. Rovira-Garcia, "Assessment of noise of MEMS IMU sensors of different grades for GNSS/IMU navigation," *Sensors*, vol. 24, no. 6, p. 1953, Mar. 2024.

[29] F. Huang, Z. Wang, L. Xing, and C. Gao, "A MEMS IMU gyroscope calibration method based on deep learning," *IEEE Trans. Instrum. Meas.*, vol. 71, pp. 1–9, 2022.
[30] P. Groves, *Book Principles of Gnss, Inertial and Multi-Sensor Integrated Navigation Systems*, 2nd ed., Norwood, MA, USA: Artech House, 2013.
[31] K.-W. Chiang et al., "Assessment for INS/GNSS/odometer/barometer integration in loosely-coupled and tightly-coupled scheme in a GNSS-degraded environment," *IEEE Sensors J.*, vol. 20, no. 6, pp. 3057–3069, Mar. 2020.
[32] B. Liang and L. Pengz, "On integrated navigation for vehicle dead reckoning," *Comput. Meas. Control*, vol. 18, pp. 2379–2384, Oct. 2010.
[33] L. Wang, X. Niu, T. Zhang, H. Tang, and Q. Chen, "Accuracy and robustness of ODO/NHC measurement models for wheeled robot positioning," *Measurement*, vol. 201, Sep. 2022, Art. no. 111720.
[34] J. T. Curran, "Enhancing weak-signal carrier phase tracking in GNSS receivers," *Int. J. Navigat. Observ.*, vol. 2015, pp. 1–15, Nov. 2015.
[35] G. Xie, *Principles of Gps and Receiver Design*, vol. 7. Beijing, China: House of Electronics Industry, 2009, pp. 61–63.
[36] P. L. Kazemi, "Optimum digital filters for GNSS tracking loops," in *Proc. 21st Int. Tech. Meeting Satell. Division Inst. Navigat. (ION GNSS)*, 2008, pp. 2304–2313.
[37] P. L. Kazemi and C. O'Driscoll, "Comparison of assisted and stand-alone methods for increasing coherent integration time for weak GPS signal tracking," in *Proc. 21st Int. Tech. Meeting Satell. Division Inst. Navigat. (ION GNSS)*, 2008, pp. 1730–1740.
[38] Y. Ban, X. Niu, T. Zhang, Q. Zhang, and J. Liu, "Modeling and quantitative analysis of GNSS/INS deep integration tracking loops in high dynamics," *Micromachines*, vol. 8, no. 9, p. 272, Sep. 2017.
[39] *Spirent GSS6450 Multi-Frequency Record & Playback System*, Spirent Commun. plc, Crawley, U.K., Mar. 2022.
[40] X. Feng, T. Zhang, T. Lin, H. Tang, and X. Niu, "Implementation and performance of a deeply-coupled GNSS receiver with low-cost MEMS inertial sensors for vehicle urban navigation," *Sensors*, vol. 20, no. 12, p. 3397, Jun. 2020.
[41] R. Ong, "Reliability of combined GPS/GLONASS ambiguity resolution," in *Masters Abstracts International*, vol. 49. Ann Arbor, MI, USA: University Microfilms International (UMI), 2010.

Tisheng Zhang (Member, IEEE) received the B.Sc. and Ph.D. degrees in communication and information systems from Wuhan University, Wuhan, China, in 2008 and 2013, respectively.

He is currently a Professor with the GNSS Research Center, Wuhan University. He was a Post-Doctoral Researcher at Hong Kong Polytechnic University, Hong Kong, from 2017 to 2018. His research interests focus on the fields of GNSS receivers, multisensor positioning, and robot navigation.

Huilin Shi received the B.E. degree from Wuhan University, China, in 2024, where she is currently pursuing the M.E. degree with the GNSS Research Center.

Her primary research interests include GNSS receivers and multisensor ultratightly coupled integration navigation.

Liqiang Wang (Graduate Student Member, IEEE) received the B.E. and M.E. degrees from Wuhan University, China, in 2020 and 2023, respectively, where he is currently pursuing the Ph.D. degree with the GNSS Research Center.

His primary research interests include GNSS/INS integration, visual SLAM, and multisensor fusion navigation systems.

Xin Feng received the M.E. and Ph.D. degrees from Wuhan University, Wuhan, China, in 2021 and 2025, respectively.

His primary research interests include GNSS receivers, GNSS high-precision positioning, and multisensor ultratightly coupled integration.

Yuepei Shi received the B.E. degree in communication engineering from Wuhan University, Wuhan, China, in 2024, where he is currently pursuing the M.E. degree with the GNSS Research Center.

His primary research interests focus on GNSS receivers and multisensor deep integration.

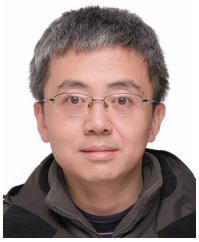

Xiaoji Niu (Member, IEEE) received the bachelor's and Ph.D. degrees (Hons.) from the Department of Precision Instruments, Tsinghua University, Beijing, China, in 1997 and 2002, respectively.

He is a Professor at the GNSS Research Center, Wuhan University, Wuhan, China. He was a Post-Doctoral Researcher at the University of Calgary, Calgary, AB, Canada, and a Senior Scientist at SiRF Technology Inc., San Jose, CA, USA He is currently leading the Integrated and Intelligent Navigation (i2Nav) Group. He has authored over 200 academic papers and owns over 30 patents. His research interests focus on GNSS/INS integration, low-cost navigation sensor fusion, and relevant new applications.